Research Article Vol. 32, No. 2 / 15 Jan 2024 / Optics Express 2106
Optics EXPRESS

AlInAsSb Geiger-mode SWIR and eSWIR SPADs with high avalanche probability

Daniel J. Herrera,[1] Adam A. Dadey,[1] Stephen D. March,[2] Seth R. Bank,[2] and Joe. C. Campbell[1,*]

[1]Department of Electrical and Computer Engineering, University of Virginia, Charlottesville, Virginia 22903, USA
[2]Department of Electrical and Computer Engineering, University of Texas, Austin, Texas 78758, USA
[*]jcc7s@virginia.edu

Abstract: Single-photon avalanche diodes (SPADs) that are sensitive to photons in the Short-wave infrared and extended short-wave infrared (SWIR and eSWIR) spectra are important components for communication, ranging, and low-light level imaging. The high gain, low excess noise factor, and widely tunable bandgap of $Al_xIn_{1-x}As_ySb_{1-y}$ avalanche photodiodes (APDs) make them a suitable candidate for these applications. In this work, we report single-photon-counting results for a separate absorption, charge, and multiplication (SACM) Geiger-mode SPAD within a gated-quenching circuit. The single-photon avalanche probabilities surpass 80% at 80 K, corresponding with single-photon detection efficiencies of 33% and 12% at 1.55 µm and 2 µm, respectively.

1. Introduction

In the SWIR (0.95-1.7 µm) and eSWIR (1.7-2.2 µm) spectra, there are numerous applications for which the development of single-photon-counting (SPC) detectors is crucial. At 1.55 µm, single-photon detectors are an important component of next-generation long-distance information networks using quantum key distribution [1,2]. At wavelengths between 1.8-2.0 µm and beyond, single-photon detection is a key requirement for developing various low-light-level imaging and sensing applications, including eye-safe LIDAR [3,4]. Thus far, the best-performing SPC detectors have been superconducting nanowire single-photon photodetectors (SNSPDs) that require extreme cryogenic temperatures [5,6]. Single-photon avalanche detectors are a promising alternative to SNSPDs for some applications since they offer suitably high detection efficiency and low noise at higher operating temperatures. For 1.55 µm applications, planar Geiger-mode InGaAs/InP SPADs have demonstrated state-of-the-art performance [7,8]. However, their absorption cuts off around 1.8 µm, making them less suitable for eSWIR applications. Meanwhile, the only significant SPC results in this spectrum have been realized using HgCdTe linear-mode SPAD arrays [9,10]. Despite HgCdTe's outstanding performance, it has several challenges compared to III-V materials, such as narrow growth windows and difficulty controlling p-type doping concentrations, which can limit reproducibility and the range of possible device designs [11].

The $Al_xIn_{1-x}As_ySb_{1-y}$ digital alloy is a quaternary III-V material structure with several qualities that make it suitable for low-noise infrared detection, including single-photon applications. By altering the percentage of Al in the quaternary, its cutoff wavelength can be broadly tuned from sub-micron wavelengths [12] out to 2 µm [13], and beyond into the MWIR spectrum, as far as 3.5 µm [14] while exhibiting high gain with low excess noise factors comparable to that of Si APDs. In the following, $Al_xIn_{1-x}As_ySb_{1-y}$ will be referred to by its Al concentration as Al_xInAsSb. Compared to MWIR HgCdTe APDs, Al_xInAsSb structures can be fabricated using mature semiconductor processing techniques and grown lattice-matched to the more commercially

#513956 https://doi.org/10.1364/OE.513956
Journal © 2024 Received 21 Nov 2023; revised 20 Dec 2023; accepted 20 Dec 2023; published 5 Jan 2024

Optics EXPRESS

available GaSb substrates, as opposed to the less common CdZnTe wafers which are preferred for HgCdTe lattice-matched epitaxy [15,16].

In this work, the SPC performance of an $Al_{0.3}InAsSb$ Geiger-mode SPAD is characterized for 1.55 µm and 2 µm illumination. To characterize the material's baseline performance, these measurements were performed with a gated-quenching circuit, in which a 5 ns gated voltage pulse pushes the device into Geiger mode at a repetition rate of 10 kHz. This is the first report of III-V compound Geiger-mode SPC results performed at 2 µm illumination.

2. Experimental details

The SACM SPAD in this work was grown as a digital alloy on an n-type GaSb substrate via molecular beam epitaxy, as shown in Fig. 1(a) [17]. This design features a continuously graded charge layer whose bandgap is between that of the $Al_{0.3}InAsSb$ absorber and the $Al_{0.7}InAsSb$ multiplication layer, allowing photogenerated electrons to transit into the multiplication region while minimizing band-to-band tunneling [13]. A double-mesa structure was etched using standard photolithography and wet etching using citric acid, phosphoric acid, hydrogen peroxide, and water. The wider bottom mesa (80 µm diameter) was etched slightly into the n-contact layer, while the narrower top mesa (70 µm diameter) was etched slightly into the multiplication region to confine the electric field away from the sidewall of that layer. Circular ring contacts of Ti/Au were deposited using e-beam evaporation, as shown in Fig. 1(b). The mesa sidewalls were then passivated by spinning and patterning a 500 nm thick layer of SU-8 photoresist.

Layer	Thickness (nm)	Doping (cm^{-3})
p^+-GaSb (cap)	30	$p = 5x10^{18}$
p^+-$Al_{0.7}InAsSb$ (contact)	50	$p > 1x10^{18}$
p-$Al_{0.7}InAsSb$ (blocking)	100	$p = 1x10^{18}$
p-$Al_{0.3}InAsSb$ (blocking)	100	$p = 1x10^{18}$
i-$Al_{0.3}InAsSb$ (absorption)	1000	UID
p-$Al_{0.3\text{-}0.7}InAsSb$ (grading)	200	$p = 6x10^{16}$
p-$Al_{0.7}InAsSb$ (charge)	80	$p = 1x10^{17}$
i-$Al_{0.7}InAsSb$ (multiplication)	500	UID
n^+-$Al_{0.7}InAsSb$ (contact)	400	$n > 1x10^{18}$
n-GaSb Substrate		$n > 1x10^{17}$

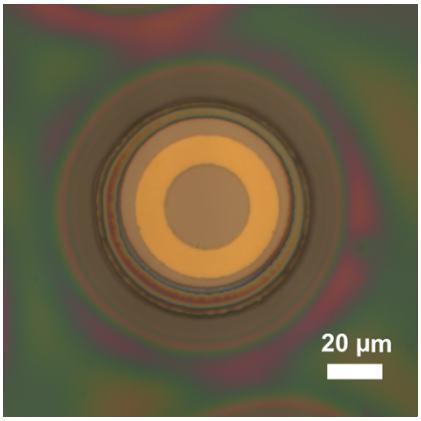

(a) (b)

Fig. 1. (a) Diagram of the epitaxial layer structure of the $Al_{0.3}InAsSb$ digital alloy SACM SPAD. (b) Microscope image of SU-8 passivated, double-mesa photodetector with upper and lower mesa diameters of 70 µm and 80 µm, respectively.

Figure 2 shows a diagram of the gated quenching apparatus used for SPAD characterization. A 30 kΩ resistor, R_L, was placed between the DC bias voltage and the cathode to protect the device under test by reducing the overall current flow through the SPAD while operating in Geiger mode. A 27 pF gate capacitor, C_g, is also included to de-couple the DC bias and the pulsed voltage arriving from the pulse generator. The resulting RC time constant $R_L C_g$ (0.81 µs) was chosen to be significantly longer than the gate pulse width (5 ns) but shorter than the gate period (100 µs). This was done to ensure that the avalanche quenching is due only to the end of the gate pulse and to reduce the residual charge at the start of the next clock cycle. To cancel the effect of capacitive transients in the output signal, a matched delay line comprised of an open coaxial cable on the input and a shorted coaxial cable on the output was also included [18]. The cryo-chamber

Optics EXPRESS

was cooled to the desired temperature using a vacuum pump to reduce the pressure to under 10 mTorr before flowing liquid nitrogen. A continuous-wave distributed feedback laser was coupled into the cryo-chamber using single-mode optical fiber and coupled to the front surface of the photodetector through a cleaved fiber. The fiber was aligned by illuminating the SPAD with an arbitrary optical power while biased above its punch-through voltage and then maximizing the photocurrent. A digital variable optical attenuator (VOA) was then used to reduce the optical power level to single-photon levels, using the responsivity of the device under test as a calibration. A photon level of 0.5 photons/pulse was chosen, which for continuous-wave illumination and a 5 ns pulse width, corresponds with a photon flux of 10^8 photons/sec, which is equivalent to 12.8 pW of incident optical power.

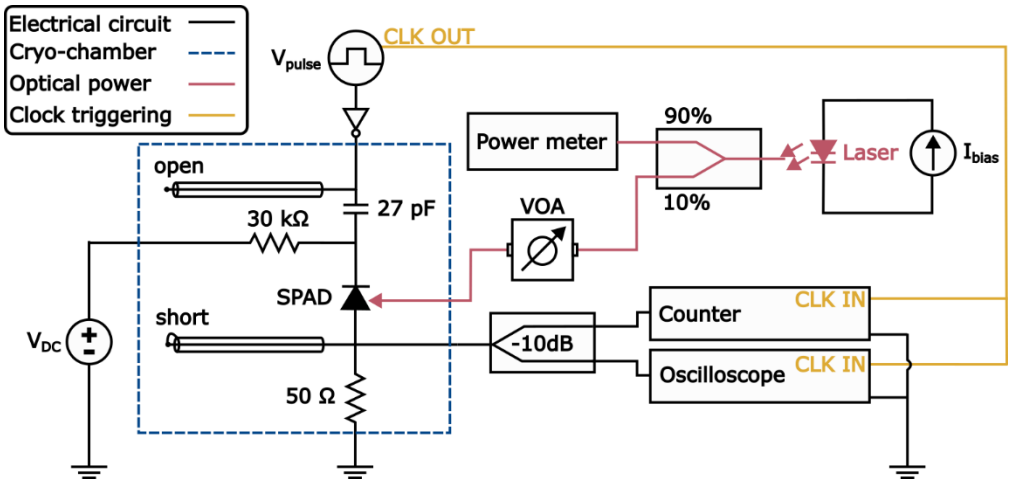

Fig. 2. Diagram of the single-photon-counting measurement system and gated-quenching circuit.

To perform single-photon measurements, a Keithley 2400 SourceMeter was used to reverse bias the SPAD to 2 V below its breakdown voltage which was arbitrarily defined as the voltage where the dark current exceeds 1 μA. The pulse generator was then used to intermittently push the device into Geiger-mode operation, with a chosen over-bias voltage, V_{OB}, at a repetition rate of 10 kHz. The over-bias voltage is defined as $\boldsymbol{V_{OB}} = |\boldsymbol{V_{DC}} + \boldsymbol{V_{pulse}} - \boldsymbol{V_{BD}}|$, where V_{DC} is the applied DC bias, V_{pulse} is the amplitude of the pulsed voltage, and V_{BD} is the breakdown voltage of the SPAD. The output signal from the SPAD is split, with 90% of the signal going to a HydraHarp 400 Time-Correlated Single-Photon Counting system, which histograms the resulting counts with a resolution of 1 ps. A Constant Fraction Discriminator (CFD) level was used to distinguish avalanche pulses from the background noise. The remaining 10% of the output signal was connected to an oscilloscope, allowing real-time observation of the necessary CFD level. The CFD was chosen to be slightly larger than the residual capacitive transients for all measurements. Since the matched delay line mostly cancels these transients, the CFD level could be set between 15-25 mV for most V_{OB} values.

To characterize the effects of afterpulsing on the dark count rate, a double-pulse method was used [19]. The SPAD was biased into Geiger-mode twice in each clock cycle by applying two separate 5 ns wide gates, during which mid-gap trap states are filled then subsequently released, respectively. Any excess counts measured in the second gate are then attributed to afterpulsing caused by these de-trapping events. The set delay time between the two gates, referred to as the ‘hold-off time’, was increased exponentially from 100 ns to 1 ms. This process mimics how the clock period varies when the SPAD is operated at different repetition rates while providing

Optics EXPRESS

enough time for the trap states to fully empty before the first pulse of the next clock cycle. Within each clock cycle, the SPAD was illuminated at a few-photon level during the first pulse with a 400 ps wide optical pulse from a 1.55 µm laser, while for the second pulse, the SPAD was in the dark. A DC bias current slightly above threshold was applied to the DFB laser, while a pulsed voltage synchronized to the SPAD's first gate pulse was separately applied using an external bias T adapter. For all measured temperatures, the over-bias level was chosen such that the dark count probability was approximately 20%.

3. Results

3.1. Current-voltage (I-V) versus temperature

Figure 3 shows the I-V characteristics of the double-mesa SPAD with upper and lower mesa diameters of 70 µm and 80 µm, respectively. As shown, the dark current decreases to below 10 nA at 180 K, at which point the dark current is low enough that counts can be measured reliably. For the top curves, the SPAD was illuminated with an optical power on the order of ~5 µW to demonstrate the punch-through voltage, which is approximately -22 V. This optical power level was then attenuated to the single-photon level, using the detector's responsivity as the reference. The responsivity was obtained by measuring the photocurrent at −23 V using several known optical power levels and was found to be 0.76 A/W at 1.55 µm. Therefore, the photocurrent at this applied bias is expected to be 9.8 pA when the desired 12.8 pW of optical power is incident upon the SPAD at 0.5 photons/pulse illumination. An attenuation level of approximately 55 dB was set on the VOA to achieve this photon input condition. The 1.55 µm and 2 µm external quantum efficiencies (EQE) of this device at 160 K and −23 V have previously been reported to be 61% and 20%, respectively [20]. Using the measured responsivity, a gain of 1.45 can be calculated. Therefore, the unity-gain EQE values of the device at these wavelengths are 42% and 13.8%, which set the upper limit for measurable detection efficiency.

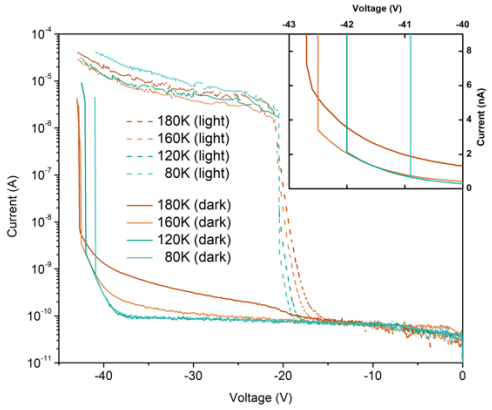

Fig. 3. Dark and 1.55 µm laser-illuminated current-voltage measurements of the SPAD at various temperatures. (inset) Magnified view of dark current levels versus temperature immediately below the breakdown voltage.

3.2. Dark count rate (DCR)

The DCR curves shown in Fig. 4 were calculated as

$$DCR = \frac{-\ln(1 - P_d)}{\tau_p}, \tag{1}$$

Optics EXPRESS

where P_d is the dark count probability, and τ_p is the gated pulse width. Generally, the DCR increases more rapidly at lower V_{OB}, before reaching a more consistent slope at moderate V_{OB}. A larger V_{OB} is required at lower temperatures to compensate for the electrons' lower average thermal energy. The order of magnitude of the absolute DCR can be primarily attributed to the higher dark currents due to the device area, which is relatively large for a SPAD. Therefore, the measured DCRs were normalized based on the size of the top diameter. Since the electric field should be confined to the diameter of the top mesa, only electrons within the top diameter should be accelerated into the multiplication layer, where they undergo the impact ionization required for an avalanche event. This normalized DCR decreases by about an order of magnitude for every 40 K of cooling, down to approximately 1 kHz/μm^2 for moderate over-bias values at 80 K.

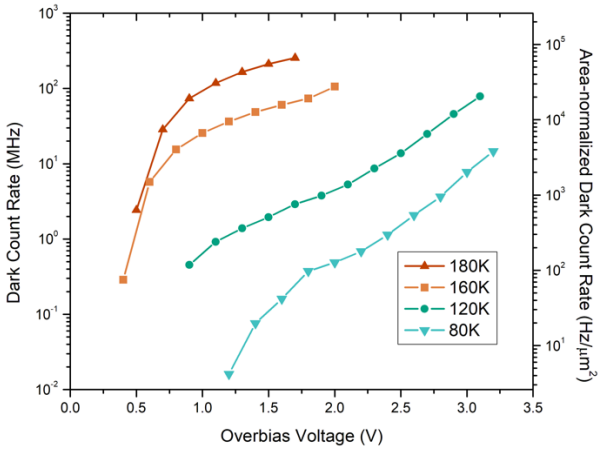

Fig. 4. DCR and area normalized DCR as a function of V_{OB} for all measured temperatures.

The 80 K normalized DCR results are comparable to HgCdTe 2×2 pixels at the same temperature, which have demonstrated DCRs between 200 kHz and 1 MHz for an illuminated diameter of 16 μm, corresponding to a normalized DCR of about 1-5 kHz/μm^2 [10]. SPADs with a larger bandgap, such as planar InGaAs/InP [7], have a lower DCR, in part due to the larger bandgap of their absorber. Beyond shrinking the device size, the absolute DCR shown here could also be reduced at a circuit design level, such as by using a balanced receiver layout containing 2 SPADs, with or without a sinusoidal gating scheme [20,21].

3.3. Photon detection efficiency (PDE)

The photon detection efficiency was calculated as

$$PDE = 1 - \left(\frac{1 - P_{av}}{1 - P_d}\right)^{\frac{1}{\mu}}, \tag{2}$$

where μ is the average number of photons per pulse and P_{av} is the total avalanche probability, which is the sum of P_d and the photon count probability P_{ph}. The PDE versus DCR results for λ = 1.55 μm are shown in Fig. 5(a).

As the temperature decreases, the highest measured PDE also increases, with maximum values of 19%, 27%, and 33% at temperatures of 160 K, 120 K, and 80 K. Figure 5(b) demonstrates how P_d and P_{ph} evolve with increasing over-bias. At higher operating temperatures, the maximum PDE is likely DCR-limited since P_d approaches unity before P_{ph} does for large V_{OB}. Conversely, at lower temperatures where the DCR is lower, P_{ph} can assume a larger percentage of P_{av}, which then increases PDE.

Optics EXPRESS

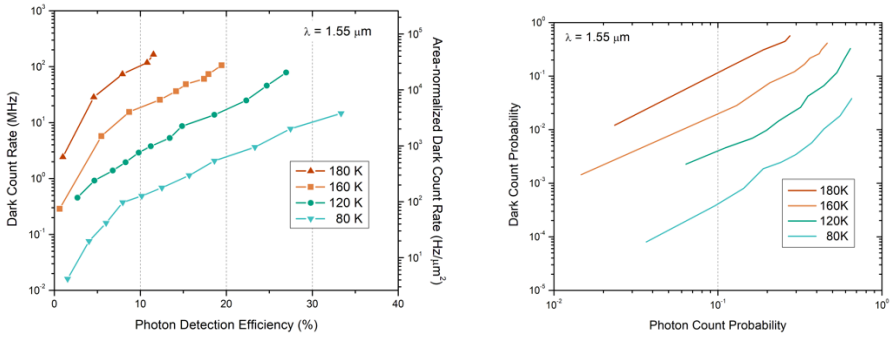

Fig. 5. (a) 1.55 μm SPDE versus area normalized DCR for the $Al_{0.3}InAsSb$ SPAD over a range of temperatures. (b) 1.55 μm dark count probability versus photon count probability over a range of temperatures.

Likewise, Fig. 6 shows PDE versus DCR for the device in response to single-photon illumination at λ = 2 μm. Just as is the case for 1.55 μm, the PDE is likely DCR-limited at higher temperatures. Likewise, the photon count probability increases at lower temperatures, with a maximum PDE value of 12%. As shown in Fig. 6(b), a similar trend is also indicated for the count probabilities, where the PDE is limited by dark counts at higher temperatures. For any PDE value measured at 2 μm, the corresponding DCR value does not match the 1.55 μm measurement because the avalanche probability scales more directly with over-bias rather than the PDE. Therefore, each increase in overbias for 2 μm corresponds with a smaller increase in photon-induced avalanche events, thus resulting in a more vertical slope in the PDE versus DCR plot. The larger dark count probabilities compared to the 1.55 μm results are due to larger over-biases required to obtain photon counts.

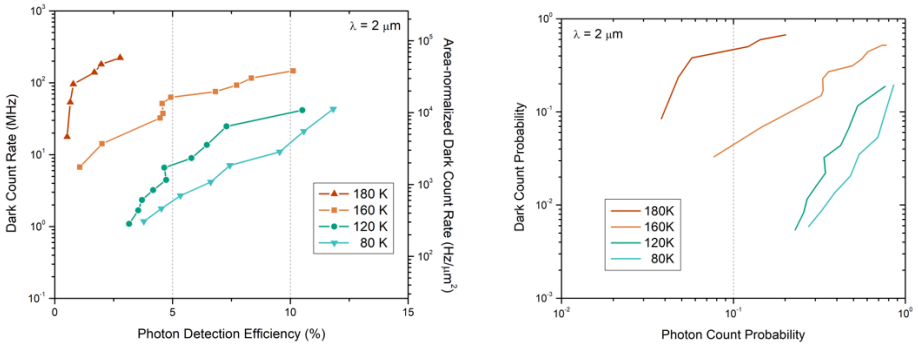

Fig. 6. (a) 2 μm SPDE vs area normalized DCR for the $Al_{0.3}InAsSb$ SPAD over a range of temperatures. (b) 2 μm dark count probability versus photon count probability over a range of temperatures.

The unity-gain EQE at 2 μm, and therefore the maximum PDE value, could be enhanced to around 35% by doubling the thickness of the absorber region to 2 μm [13]. However, this would come with a trade-off of higher dark current originating in the absorber. Alternatively, the maximum PDE could be increased without increasing dark current by applying a photon-trapping structure on the front surface of the detector, such as a 2D gold grating, which has been shown to strongly enhance the EQE of an APD with a thin absorber [22]. With these EQE enhancements and measures to reduce the dark current, further decreasing the Al composition in the absorber could enable AlInAsSb to be a suitable material for Mid-wave Infrared (MWIR) single photon

Optics EXPRESS

counting. For example, at an Al percentage of 5%, a unity-gain EQE of 24% at 3 µm has been reported [14].

3.4. Afterpulsing

The measured afterpulsing probability, P_{AP}, and afterpulsing rate are shown in Fig. 7(a). The afterpulsing rate was calculated as

$$P_{AP} = \frac{P_{av,2} - P_d}{1 - P_d}, \tag{3}$$

where $P_{av,2}$ is the total avalanche probability measured in the second pulse only.

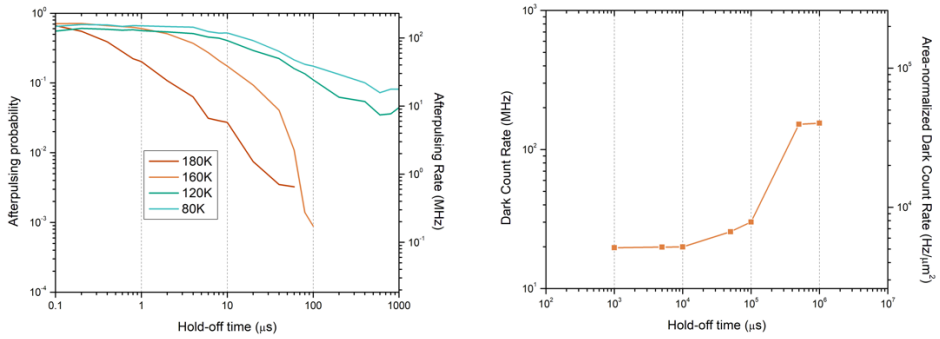

Fig. 7. (a) Afterpulsing probability and afterpulsing rate versus hold-off time for a range of temperatures, measured at a repetition rate of 1 kHz. (b) DCR versus repetition rate at a temperature of 160 K.

P_{AP} decreases faster with increasing hold-off time at higher temperatures since the higher thermal energy causes trapped carriers to be released more quickly. The effect of afterpulsing on the DCR value measured at 160 K is shown in Fig. 7(b). At frequencies lower than 100 kHz, the DCR is independent of the repetition rate, indicating that the effect of afterpulsing is negligible. To reduce the afterpulsing probability, the amount of current flowing through the SPAD during an avalanche should be reduced. This can be achieved by using a gate pulse shorter than 5 ns. However, this may come with the trade-off of lower PDE since it would decrease the time an avalanche has to increase above the CFD level. Afterpulsing may also be reduced by applying a higher DC bias since a higher electric field during the off-state would more effectively cause the trapped carriers to be released. A circuit with a passive quench and active reset can further reduce the effect of afterpulsing by lowering the total charge flow during an avalanche event, which decreases the amount of charge trapping that occurs [23].

4. Conclusion

This work presents SWIR and eSWIR single-photon counting results for a gated-quenched $Al_{0.3}InAsSb$ SACM SPAD. Avalanche breakdown probabilities above 80% were measured, with 1.55 µm PDE values of 19% at 160 K and 33% at 80 K. Additionally, we report the first III-V Geiger-mode single photon counting results at 2 µm, with a PDE of 12% at 80 K. When normalized by area, the DCR values are comparable to linear-mode HgCdTe SPAD arrays. These results suggest that with further optimization of the device structure, SPADs grown using the AlInAsSb digital alloy could be candidates for single photon counting applications in the SWIR and eSWIR spectral regions.

Funding. QC82, Inc. (002248); National Science Foundation (1838435).

Optics EXPRESS

Acknowledgements. This work was supported by QC82. Inc. under contract 002248 and the National Science Foundation under contract 1838435.

Disclosures. The authors have no conflicts of interest to disclose.

Data availability. Data underlying the results presented in this paper are publicly available and may be obtained from the authors upon reasonable request.

References

1. F. Ceccarelli, G. Acconcia, A. Gulinatti, *et al.*, "Recent Advances and Future Perspectives of Single-Photon Avalanche Diodes for Quantum Photonics Applications," Adv. Quantum Technol. **4**(2), 2000102 (2021).
2. E. Diamanti, H.-K. Lo, B. Qi, *et al.*, "Practical challenges in quantum key distribution," npj Quantum Inf **2**(1), 16025 (2016).
3. R. H. Hadfield, J. Leach, F. Fleming, *et al.*, "Single-photon detection for long-range imaging and sensing," Optica **10**(9), 1124 (2023).
4. F. Villa, F. Severini, F. Madonini, *et al.*, "SPADs and SiPMs Arrays for Long-Range High-Speed Light Detection and Ranging (LiDAR)," Sensors **21**(11), 3839 (2021).
5. I. Esmaeil Zadeh, J. Chang, J. W. N. Los, *et al.*, "Superconducting nanowire single-photon detectors: A perspective on evolution, state-of-the-art, future developments, and applications," Appl. Phys. Lett. **118**(19), 190502 (2021).
6. D. V. Reddy, R. R. Nerem, S. W. Nam, *et al.*, "Superconducting nanowire single-photon detectors with 98% system detection efficiency at 1550 nm," Optica **7**(12), 1649–1653 (2020).
7. F. Signorelli, F. Telesca, E. Conca, *et al.*, "Low-Noise InGaAs/InP Single-Photon Avalanche Diodes for Fiber-Based and Free-Space Applications," IEEE J. Sel. Top. Quantum Electron. **28**(2: Optical Detectors), 1–10 (2022).
8. J. Zhang, M. A. Itzler, H. Zbinden, *et al.*, "Advances in InGaAs/InP single-photon detector systems for quantum communication," Light: Sci. Appl. **4**(5), e286 (2015).
9. P. D. Anderson, J. D. Beck, W. Sullivan, *et al.*, "Recent Advancements in HgCdTe APDs for Space Applications," J. Electron. Mater. **51**(12), 6803–6814 (2022).
10. X. Sun, J. B. Abshire, M. A. Krainak, *et al.*, "HgCdTe avalanche photodiode array detectors with single photon sensitivity and integrated detector cooler assemblies for space lidar applications," Opt. Eng. **58**(06), 1 (2019).
11. W. Lei, J. Antoszewski, and L. Faraone, "Progress, challenges, and opportunities for HgCdTe infrared materials and detectors," Appl. Phys. Rev. **2**(4), 041303 (2015).
12. M. E. Woodson, M. Ren, S. J. Maddox, *et al.*, "Low-noise AlInAsSb avalanche photodiode," Appl. Phys. Lett. **108**(8), 081102 (2016).
13. A. H. Jones, S. D. March, S. R. Bank, *et al.*, "Low-noise high-temperature AlInAsSb/GaSb avalanche photodiodes for 2-µm applications," Nat. Photonics **14**(9), 559–563 (2020).
14. A. A. Dadey, J. A. McArthur, A. Kamboj, *et al.*, "High-gain low-excess-noise MWIR detection with a 3.5-µm cutoff AlInAsSb-based separate absorption, charge, and multiplication avalanche photodiode," APL Photonics **8**(3), 036101 (2023).
15. R. Gu, J. Antoszewski, W. Lei, *et al.*, "MBE growth of HgCdTe on GaSb substrates for application in next generation infrared detectors," J. Cryst. Growth **468**, 216–219 (2017).
16. F. E. Arkun, D. D. Edwall, J. Ellsworth, *et al.*, "Characterization of HgCdTe Films Grown on Large-Area CdZnTe Substrates by Molecular Beam Epitaxy," J. Electron. Mater. **46**(9), 5374–5378 (2017).
17. S. J. Maddox, S. D. March, and S. R. Bank, "Broadly Tunable AlInAsSb Digital Alloys Grown on GaSb," Cryst. Growth Des. **16**(7), 3582–3586 (2016).
18. D. S. Bethune and W. P. Risk, "An autocompensating fiber-optic quantum cryptography system based on polarization splitting of light," IEEE J. Quantum Electron. **36**(3), 340–347 (2000).
19. S. Cova, A. Lacaita, and G. Ripamonti, "Trapping phenomena in avalanche photodiodes on nanosecond scale," IEEE Electron Device Lett. **12**(12), 685–687 (1991).
20. J. C. Campbell, W. Sun, Z. Lu, *et al.*, "Common-Mode Cancellation in Sinusoidal Gating With Balanced InGaAs/InP Single Photon Avalanche Diodes," IEEE J. Quantum Electron. **48**(12), 1505–1511 (2012).
21. Z. Lu, W. Sun, J. C. Campbell, *et al.*, "Pulsed Gating With Balanced InGaAs/InP Single Photon Avalanche Diodes," IEEE J. Quantum Electron. **49**(5), 485–490 (2013).
22. D. Chen, S. D. March, A. H. Jones, *et al.*, "Photon-trapping-enhanced avalanche photodiodes for mid-infrared applications," Nat. Photonics **17**(7), 594–600 (2023).
23. M. Liu, C. Hu, J. C. Campbell, *et al.*, "Reduce Afterpulsing of Single Photon Avalanche Diodes Using Passive Quenching With Active Reset," IEEE J. Quantum Electron. **44**(5), 430–434 (2008).